ACS NANO

Cite This: *ACS Nano* 2019, 13, 10359−10365

www.acsnano.org

ARTICLE

Nanoscale Photovoltaic Responses in 3D Radial Junction Solar Cells Revealed by High Spatial Resolution Laser Excitation Photoelectric Microscopy

Huili Zhang,[†] Yakui Lei,[‡] Qiang Zhu,[†] Tong Qing,[†] Ting Zhang,[‡] Wanghao Tian,[†] Matthias Lange,[§] Meiping Jiang,[†] Chao Han,[†] Jun Li,[†] Dieter Koelle,[§] Reinhold Kleiner,[§] Wei-Wei Xu,[†] Yonglei Wang,[†] Linwei Yu,[*,‡] Huabing Wang,[*,†] and Peiheng Wu[†]

[†]Research Institute of Superconductor Electronics (RISE)/School of Electronics Science and Engineering, Nanjing University, Nanjing, 210023, People's Republic of China

[‡]National Laboratory of Solid State Microstructures/School of Electronics Science and Engineering/Collaborative Innovation Center of Advanced Microstructures, Nanjing University, Nanjing, 210093, People's Republic of China

[§]Physikalisches Institut and Center for Quantum Science in LISA+, Universität Tübingen, Tübingen, 72072, Germany

Supporting Information

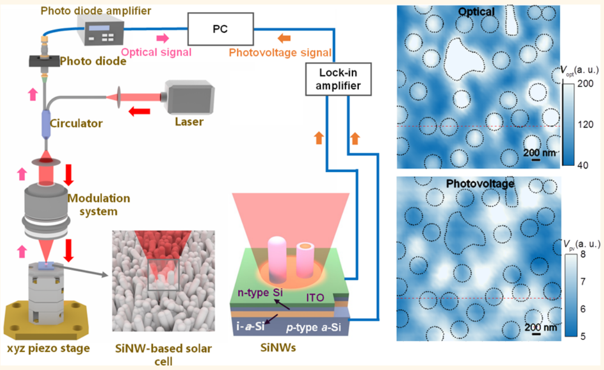

ABSTRACT: **The actual light absorption photovoltaic responses realized in three-dimensional (3D) radial junction (RJ) units can be rather different from their planar counterparts and remain largely unexplored. We here adopt a laser excitation photoelectric microscope (LEPM) technology to probe the local light harvesting and photoelectric signals of 3D hydrogenated amorphous silicon (a-Si:H) RJ thin film solar cells constructed over a Si nanowire (SiNW) matrix, with a high spatial resolution of 600 nm thanks to the use of a high numerical aperture objective. The LEPM scan can help to resolve clearly the impacts of local structural damages, which are invisible to optical and SEM observations. More importantly, the high-resolution photoelectric mapping establishes a straightforward link between the local 3D geometry of RJ units and their light conversion performance. Surprisingly, it is found that the maximal photoelectric signals are usually recorded in the void locations among the standing SiNW RJs, instead of the overhead positions above the RJs. This phenomenon can be well explained and reproduced by finite element simulation analysis, which highlights unambiguously the dominant contribution of inter-RJ-unit scattering against direct mode incoupling in the 3D solar cell architecture. This LEPM mapping technology and the results help to achieve a straightforward and high-resolution evaluation of the local photovoltaic responses among the 3D RJ units, providing a solid basis for further structural optimization and performance improvement.**

KEYWORDS: *solar cells, radial junction, silicon nanowires, photoelectric microscopy, photovoltaic signals, light trapping and absorption*

The development of high-efficiency, low-cost, lightweight, and flexible thin film solar cells has attracted tremendous research efforts in recent years.[1−8] Three-dimensional (3D) radial junction (RJ) architectures, for instance, hydrogenated amorphous silicon (a-Si:H) thin film solar cells, are particularly advantageous for achieving a strong light-trapping and absorption performance, where the light absorption length is decoupled from the electric separation distance.[9−14] This has proven useful to reduce the absorber material usage,[5] improve light-soaking stability,[15] and achieve an excellent mechanical robustness on soft substrates.[16] However, an optimal 3D solar cell design requires still a profound understanding, both theoretically and experimentally, of the exact light absorption distribution realized among the

Received: May 28, 2019
Accepted: September 3, 2019
Published: September 3, 2019

DOI: 10.1021/acsnano.9b04149
ACS Nano 2019, 13, 10359−10365

3D RJ units, which can be rather different from their planar counterparts.

As an ideal model system, RJ thin film solar cells can be fabricated upon standing Si nanowires (SiNWs) grown *via* a low-temperature, high-throughput, and low-cost vapor−liquid−solid (VLS) approach, catalyzed by metal droplets.[17−19] Recently, low-melting-point metals of tin (Sn),[20−23] indium,[24−26] and bismuth[27] have been adopted as alternative catalysts to replace the commonly used gold (Au) to enable a low-temperature (<350 °C) growth of SiNWs directly upon glass or wafer substrates.[22] Combined with the proper geometry, doping, and density controls, a-Si:H RJ thin film solar cells have achieved a power conversion efficiency of >8.14%, with an open-circuit voltage and short-circuit current of V_{oc} = 0.8 V and J_{sc} = 16.1 mA/cm^2, respectively.[15] In order to boost the device performance further, the capability to probe directly the light-harvesting and conversion performance of individual 3D RJ units in variant local environments is definitely a prerequisite. Nanoscanning probe techniques, such as scanning Kelvin probe microscopy (SKPM)[28−30] and conductive atomic force microscopy (c-AFM),[31−33] have been used to correlate the 3D RJ morphology with the local photoelectric responses. Unfortunately, these scanning probe technologies by themselves are inefficient in scanning large areas and also limited by several issues, such as (1) the local electric contacts between the protruding 3D surfaces and the probe tips, (2) the restricted touch depth into narrow valley regions, and (3) the shedding of light to the junction that is rather different from the normal incident condition for conventional solar cells. Alternatively, electron and optical beam induced current (EBIC and OBIC) mapping techniques were used to assess the local current generation and thus assess the junction quality of a-Si:H RJ units.[24] However, the EBIC technique is fundamentally limited by the top indium tin oxide (ITO) layer, which hinders the penetration of electron beams deep enough into the buried RJ units. Although OBIC can address the photoelectric response directly under the ITO electrode layer, the limited spatial resolution (around 2 μm) can only resolve the photoelectric responses from very sparse RJ units, which is unfortunately not the optimized situation for building high-performance solar cells.

In order to obtain a high-resolution photoelectric signal mapping of the RJ units, we here adopted a laser excitation photoelectric microscope (LEPM), with a spatial resolution of 600 nm thanks to a high numerical aperture objective, to probe directly high-density SiNW RJ units under the ITO layer and extract the local optical reflection and photoelectric responses simultaneously. This nondestructive and high-resolution scanning probe technology, equivalent to a high-resolution OBIC, can help to reveal the hidden electric damages among the RJ units, which are invisible even in the highest resolution optical examination. More importantly, the LEPM mapping provides a straightforward probe to identify the highest photoelectric response locations among the RJ units, which can be very useful for us to evaluate the detailed contributions of different light incoupling and absorption mechanisms, and to establish a guide for further structural optimization. Combined with finite element simulation analysis, it is shown that, among the high-density RJ units, the highest light absorption and photovoltages are usually achieved in the void locations among the RJs, highlighting the importance of suitable density controls and structural design in fabricating high-performance 3D RJ solar cells.

The p-type doped SiNWs were grown *via* a tin (Sn)-catalyzed VLS growth in a plasma-enhanced chemical vapor deposition (PECVD) system, by using a mixture gas of SiH_4 and H_2-diluted $(CH_3)_3B$ on Corning glass coated with a transparent conductive aluminum-doped zinc oxide layer. After the SiNW growth, an intrinsic a-Si:H layer and then an n-type doped a-Si:H layer were deposited consecutively to form a radial p−i−n junction over the p-type SiNWs. Finally, an 80 nm ITO layer was sputtered through shadow mask to form the top electrode, which contacts the solar cells. The details of the RJ solar cell fabrication procedure are available in our previous works.[15,34] Figure 1 shows a schematic illustration of the LEPM scanning system, where a laser diode operating at 638 nm wavelength is installed as the excitation source, and the laser beam is coupled into a single-mode optical fiber that connects to an optical circulator. Then it is focused onto the sample surface by a microscope objective lens with a numerical aperture of 0.55. The sample is mounted on an x−y−z piezo stage (Attocube micropositioner) that provides a spatial resolution of 200 nm at room temperatures.

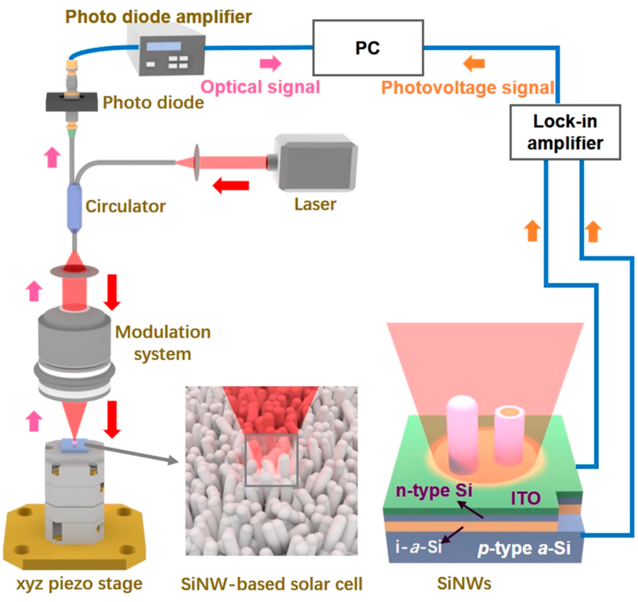

Figure 1. Schematic illustration of laser excitation photoelectric microscopy (LEPM). A modulated laser beam focused on the sample surface. The sample is fixed on a 3D micropositioner. The reflection optical signal ΔV_{opt} can be detected *via* a photodiode. The optoelectronic response ΔV_{pv}, which is generated by the perturbation of the focused beam, is detected by a lock-in amplifier at the same time.

Under the illumination of a focused laser beam, the RJs absorb the light and generate a photovoltage of ΔV_{pv} that can be detected by using a lock-in technique. In the meanwhile, the incident light can be reflected and collected by the fiber and converted into an electric signal of ΔV_{opt} by a photodiode, which can be referred to as an optical signal. In this way, a single scan of the sample surface will produce a photovoltage signal mapping and a reflected optical voltage signal mapping simultaneously, with correlated spatial information. Both of them are read out as voltage signals, but of different physical origins. The lock-in technique can help to reduce the noise and extract the photovoltage signals with a stronger contrast, as witnessed for example in Supporting Information Figure S1a

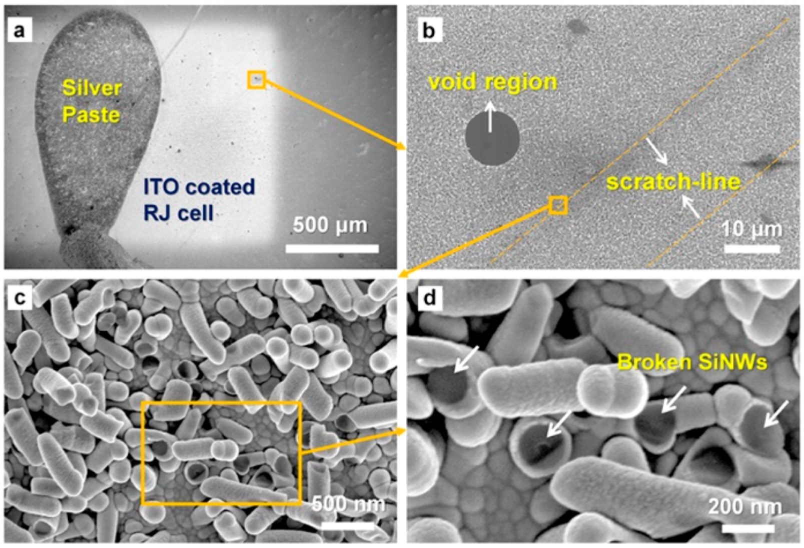

Figure 2. SEM images of a SiNW-based solar cell. (a) Overview of the solar cell. (b) Enlarged region of the SEM view with void region and scratch lines. (c and d) Close-ups of the scratch lines.

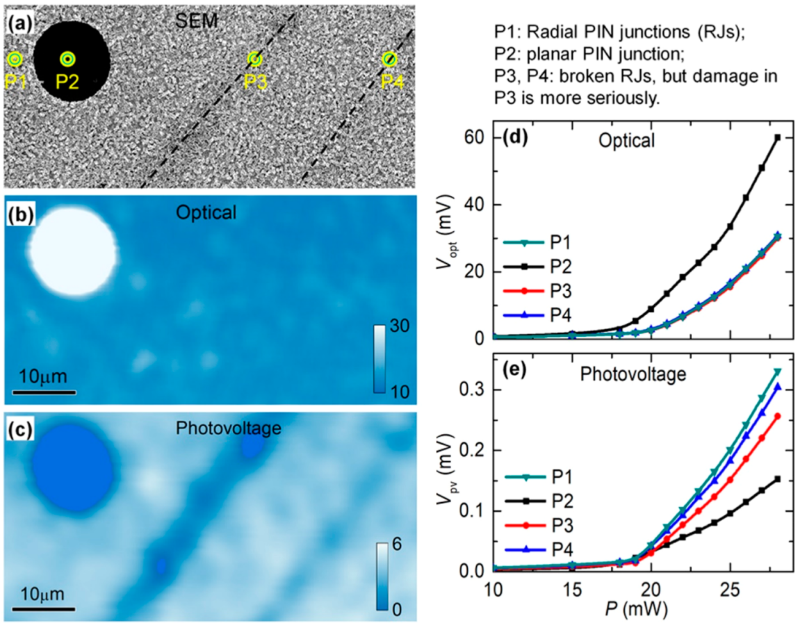
P1: Radial PIN junctions (RJs);
P2: planar PIN junction;
P3, P4: broken RJs, but damage in P3 is more seriously.

Figure 3. (a) SEM image of the scanning region, (b) optical response, and (c) optoelectronic response. (d) Optical and (e) optoelectronic response of four typical points under various laser powers.

and b, where the photovoltage mappings without or with a lock-in amplifier are presented, respectively.

The resolution of the system is mainly dependent on the spot size of the focused laser beam and the minimal step distance of the micropositioner. The diffraction-limited resolution is calculated by the diameter of the airy disc:

$$d = (1.22\lambda)/N_A \tag{1}$$

where d is the airy disk diameter, λ the wavelength of laser light, and N_A the numerical aperture of the lens. So, the laser spot size of LEPM is calculated to be about 1.4 μm for a numerical aperture N_A of 0.55 at a laser wavelength of 638 nm. In order to improve the resolution, the system adopts a short wavelength of 405 nm for the laser source, a microscope objective lens with a high numerical aperture of 0.8, and a scanning step of about 80 nm. The corresponding laser spot size is calculated to be about 600 nm.[35]

Figure 2a provides a scanning electron microscopy (SEM) image of the targeted RJ sample region, where the brighter region is covered by an ITO layer. The silver paste on top of the ITO pad to the left was used to extract the electric signals from the top ITO electrode. A selected region is marked by a yellow square, and an enlarged SEM view is presented in Figure 2b. In this region, a set of structural defects can be identified, which include (1) a void region without any SiNWs and thus no radial junction (but with a still planar PIN junction) and (2) several scratch lines where the RJ units were broken, as witnessed in Figure 2c and d. Note that the nanostructured 3D RJ units are prone to external force damage, compared to their planar counterparts, and thus their

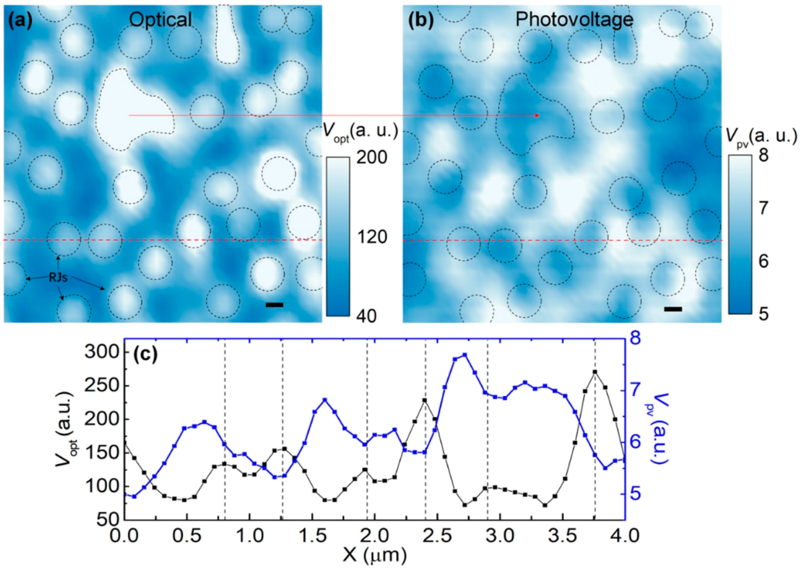

Figure 4. (a) Optical and (b) optoelectronic response of a normal region under a laser of 405 nm. The scale bar in (a) and (b) is 200 nm. (c) Optical and optoelectronic signal intensity of the dotted lines in (a) and (b).

influences or location information have to be examined or identified for quality control and optimization.

RESULTS AND DISCUSSION

First, an LEPM system with a numerical aperture N_A of 0.55 and laser wavelength of 638 nm was adopted to measure the region as shown in Figure 2b. In order to examine the correlation between the structural properties and the local optical and photoelectric responses in these defected locations, in comparison to the normal regions with intact RJ units, four typical locations were chosen as indicated in the SEM image of Figure 3a. The photovoltage and optical LEPM mappings of the same region are shown in Figure 3b and c, respectively. For the convenience of comparison, the optical signals and the photoelectric signals, as a function of increased laser power, are extracted from the four locations, numbered as P1 to P4 and plotted in Figure 3d and e. It is found that the planar PIN junction at location P2 reflects strongly due to a flat surface and thus contributes the least photoelectric signals, because of a poor light-trapping performance, compared to the RJ units in other places. On the other hand, the lower photovoltage recorded in the planar P2 region is also related to the fact that the optimized boron doping condition in crystalline p-type SiNW cores is much different from that required for the p-type a-Si layer. The latter usually requires a much higher (more than an order of magnitude) boron doping concentration to arrive at a similar doping effect in crystalline Si, due to the disorder and defective nature of the a-Si matrix.[36,37] Strikingly, the scratch-line defects, which are basically invisible in the optical mapping, can be well resolved in the electric mapping. The broken RJs in regions P3 and P4 lead to a lower photoelectric signal, compared to that of the normal region in P1, and the decreased voltage signal is more prominent in P3, as the damage there is more serious than that in P4. These findings highlight the capability of LEPM mapping in identifying the actual electric damages caused by structural defects in the RJ structure.

Furthermore, a high spatial resolution (about 600 nm) LEPM mapping was carried out in the normal RJ region with a smaller size of 4 μm wide, and the optical and photoelectric responses are provided in Figure 4a and b, respectively. Interestingly, the reflected optical response can roughly resolve the locations of the RJ units, as the brighter optical signals result from a stronger reflection from the top of the standing RJs. Note that, as the RJs are not always upright standing, the tilted ones will be detected as elongated or irregular spots. Somehow to our surprise, the photoelectric mapping reveals an inverse correlation with respect to the optical mapping. In other words, the highest photoelectric signals are usually detected at the locations with the lowest optical reflection responses, which can be better inferred from the extracted signal variation plots shown in Figure 4c. This indicates that the strongest light absorption and photoelectric generation are not accomplished over the standing RJ units, as usually expected in previous work.[38] Instead, the strongest photovoltage signals are produced in the so-called void region among RJs.

To understand this peculiar correlation phenomenon, an RJ model is established by using the RF module of the finite element simulation suite Comsol Multiphysics, in a configuration as shown in Figure 5a. Here, the SiNW core is represented by a cylinder with a radius of 20 nm and a length of 2 μm, coated with a coaxial multilayer that consists subsequently of intrinsic a-Si:H, an n-type a-Si:H layer, and ITO layers of 100, 15, and 50 nm, respectively. The single radial cell is placed at the center of a square simulation box (1.6 μm × 1.6 μm) on top of a glass substrate, with periodic conditions at the four boundary walls to represent the light absorption effect in an array. The focused laser beam light source is simulated by a y-axis-polarized light (λ = 405 nm) illuminated through a hemispherical surface with a diameter of 200 nm. Then, the light source is scanned over the RJ units, simulating the scanning of a laser beam, and the absorption realized in the active i-layer is calculated and extracted as the effective light absorption that can be converted into photoelectric signal. Figure 5a and b show the propagation of the electric field and the absorption distribution in the RJ under 405 nm incidence, respectively, while a mapping of the effective absorption by the RJ unit is shown in Figure 5c. More importantly, the highest absorption is achieved not over the RJ

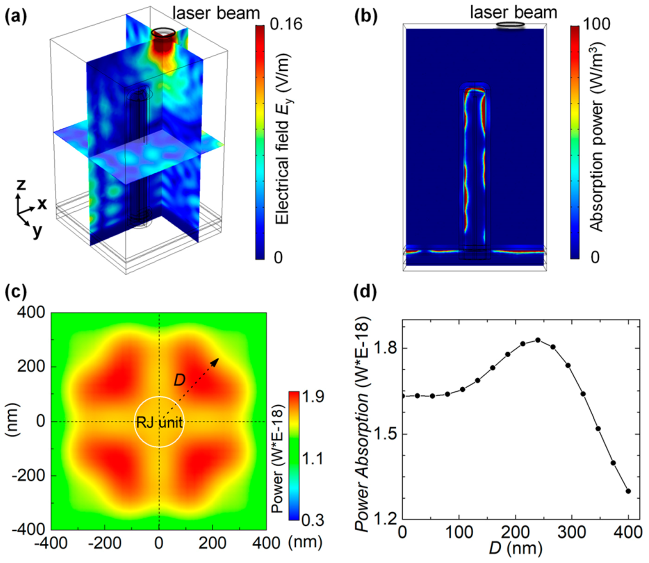

Figure 5. (a) Schematic illustration of the simulation model of a single RJ cell at 405 nm incidence light. The color cross profiles of (a) present the light field distribution in the single RJ unit. (b) Corresponding absorption profiles. The black circle out of the top border in (a) and (b) represents the incident spot laser source. (c) Effective power dissipation/absorption distribution of a single RJ cell. (d) Power absorption *vs* the distance from the RJ unit center.

unit but rather in the locations deviated 100−300 nm away from the center of the RJ, similar to the situation observed in the experimental LEPM mapping in Figure 4a and b. This spatial deviation can be better seen in Figure 5d, where the light absorption within the same distance from the RJ center is integrated/averaged and then plotted against the distance from the RJ unit center. It is found that the separation between the highest absorption location and the RJ center is around 250 nm, which explains at least qualitatively why the highest photovoltaic signals are not observed directly over the RJ units in Figure 4b. In addition, we also consider and simulate the absorption distribution around tilted RJ units; see Supporting Information Figure S2 for the light field distribution and absorption patterns realized around the RJs tilted to angles of 10, 20, and 30 deg in the $x-z$ plane. It is interesting to find that the highest absorptions are always found on both sides of the tilted RJ (and stronger around the tips of the tilted RJs), which are similar to and consistent with that found for the upright standing RJ unit, except that the spatial symmetry is broken by the tilting arrangement. These results indicate that, among the 3D RJ array, the highest light absorption is realized indeed in the region surrounded by the standing RJs, instead of in the overhead locations. Meanwhile, the impact of the light-trapping effect in the RJ matrix can also be inferred from the variation of the pitch of the RJ units, which is equivalent to changing the density of the RJ matrix. The simulated absorption patterns with different RJ-to-RJ pitch or spacing lengths, of 1400, 1600, 1800, and 3000 nm, are presented in Supporting Information Figure S3a−d, respectively. It is found that, for the pitch below 2000 nm (see Figure S3a−c), the strongest light absorption responses are realized in the regions around the RJ units. However, when the pitch increases to 3000 nm, that is, the RJ matrix becomes very sparse (see Figure S3d), the strongest absorption response region returns to overlap with the RJ unit, because the light-trapping effect diminishes rapidly in the sparse RJ matrix. This can be better understood by considering/calculating the light absorption response realized by a singly placed RJ unit (not in a matrix), under the same spot light illumination, which has been provided in Supporting Figure S4, where the periodic boundary conditions are removed and set to be absorptive. Under this situation, the strongest light absorption is indeed realized just over the RJ unit, instead of being in the nearby regions. This is because the single 3D RJ, by itself, has a much larger PIN junction volume coated upon the standing SiNW compared to that in the nearby flat region. Nevertheless, the highest absorption power realized by the single RJ (see Figure S4) is only one-third of that realized by the RJ unit placed in a matrix (see Figure 5c), emphasizing again the benefit and contributions of a strong light-trapping effect realized among the RJ arrays. These also indicate that, under normal incidence, the contribution of light trapping and absorption among RJs is more important or efficient compared to the direct light incoupling into the RJ units from the top end, which is indeed a critical message for the structural design and optimization of RJ solar cells.

CONCLUSIONS

In conclusion, high spatial resolution LEPM mapping was adopted to probe the local light harvesting and photoelectric responses of 3D a-Si:H RJ thin film solar cells, constructed over a matrix of SiNWs. The high-resolution photoelectric mapping can help to resolve the usually invisible impacts of local structural damages and establishes a direct link between the 3D geometry and their local light conversion performance. Moreover, it is found that the maximal photoelectric signal can be identified in the void locations among the standing SiNW RJs, instead in the overhead positions above RJs, which can be well explained and reproduced *via* a finite element simulation analysis that highlights the dominant contribution of light scattering among the 3D RJs against other light incoupling and absorption mechanism. These results offer an important guideline for the further structural optimization and device performance improvement.

METHODS

Device Fabrication. SiNWs were grown on the AZO glass substrate, coated with a 2 nm thick tin (Sn) layer. During the H_2 plasma at 300 °C for 90 s with flow rate, chamber pressure, and radio frequency (RF) power of 100 sccm, 260 mTorr, and 53 mW cm^{-2}, respectively, the Sn layer transformed into nanoscale droplets. Then, the substrate temperature was raised to 400 °C, and a mixture gas of 10 sccm SiH_4 and 100 H_2-diluted $(CH_3)_3B$ was introduced to trigger the growth of p-type SiNWs with a length of around 1 μm and a mean diameter of about 20 nm. After that, an intrinsic a-Si:H layer (typically ∼100 nm) and then an n-type doped a-Si:H layer (of ∼15 nm) were deposited consecutively to form a radial p−i−n junction. Finally, an 80 nm ITO layer was sputtered through a shadow mask to form the top electrode, which contacts the solar cells.

Characterization. We performed the measurements on solar cells with an LEPM system, a schematic view of which is shown in Figure 1. The laser beam was modulated on the square-wave modulation with a frequency range from 10 to 50 kHz and a voltage range from 2 to 2.18 V, corresponding to the equivalent power from 10 to 28 mW. The optical and photoelectric responses were obtained by using a lab-made voltage amplifier. The micropositioner was made by using three piezo-driven stages with sub-micrometer precision (ANPx/z101/RES, ANC350, Attocube System).

ASSOCIATED CONTENT

Supporting Information

The Supporting Information is available free of charge on the ACS Publications website at DOI: 10.1021/acsnano.9b04149.

> Figures of optoelectronic responses obtained without and with lock-in amplifier over a large region of 20-by-20 μm^2; light field distribution around a tilted RJ unit and the calculated light absorption power mapping around different tilted RJs within the $x-z$ plane; calculated effective power dissipation/absorption responses during an LEPM mapping around a single RJ cell, within a periodic array under different RJ-to-RJ spacing; effective power dissipation/absorption distribution of a single RJ cell without periodic condition at the four boundary walls (PDF)

AUTHOR INFORMATION

Corresponding Authors

*E-mail: yulinwei@nju.edu.cn.
*E-mail: hbwang@nju.edu.cn.

ORCID

Linwei Yu: 0000-0002-0801-5210
Huabing Wang: 0000-0003-4802-6077

Author Contributions

H. L. Zhang and Y. K. Lei contributed equally to this work.

Notes

The authors declare no competing financial interest.

ACKNOWLEDGMENTS

We gratefully acknowledge financial support by the National Natural Science Foundation of China (Nos. 61727805 (H.W.), 61674075 (L.Y.), 11874198 (L.Y.), 61611130069 (H.W.), and 61771235 (Y.W.)), Jiangsu Key Laboratory of Advanced Techniques for Manipulating Electromagnetic Waves, the Priority Academic Program Development of Jiangsu Higher Education Institutions (PAPD) (H.W.), the RFBR grant 17-52-12051 (R.K. and D.K.), EU-FP6-COST Action CA16218 (R.K. and D.K.), and the Deutsche Forschungsgemeinschaft *via* project KL93013/2 (R.K. and D.K.).

REFERENCES

(1) Kelzenberg, M. D.; Turner-Evans, D. B.; Kayes, B. M.; Filler, M. A.; Putnam, M. C.; Lewis, N. S.; Atwater, H. A. Photovoltaic Measurements in Single-Nanowire Silicon Solar Cells. *Nano Lett.* **2008**, *8*, 710−714.

(2) Kempa, T. J.; Cahoon, J. F.; Kim, S.-K.; Day, R. W.; Bell, D. C.; Park, H.-G.; Lieber, C. M. Coaxial Multishell Nanowires with High-Quality Electronic Interfaces and Tunable Optical Cavities for Ultrathin Photovoltaics. *Proc. Natl. Acad. Sci. U. S. A.* **2012**, *109*, 1407−1412.

(3) Tian, B. Z.; Zheng, X. L.; Kempa, T. J.; Fang, Y.; Yu, N. F.; Yu, G. H.; Huang, J. L.; Lieber, C. M. Growth of High-Density Titanium Silicide Nanowires in a Single Direction on a Silicon Surface. *Nature* **2007**, *7*, 885−889.

(4) Kim, S.-K.; Day, R. W.; Cahoon, J. F.; Kempa, T. J.; Song, K.-D.; Park, H.-G.; Lieber, C. M. Tuning Light Absorption in Core/Shell Silicon Nanowire Photovoltaic Devices through Morphological Design. *Nano Lett.* **2012**, *12*, 4971−4976.

(5) Misra, S.; Yu, L. W.; Chen, W. H.; Foldyna, M.; Roca i Cabarrocas, P. A Review on Plasma-Assisted VLS Synthesis of Silicon Nanowires and Radial Junction Solar Cells. *J. Phys. D: Appl. Phys.* **2014**, *47*, 393001.

(6) Frederiksen, R.; Tutuncuoglu, F.; Matteini, F.; Martinez, K. L.; Fontcuberta i Morral, A. Visual Understanding of Light Absorption and Waveguiding in Standing Nanowires with 3D Fluorescence Confocal Microscop. *ACS Photonics* **2017**, *4*, 2235−2241.

(7) Mann, S. A.; Oener, S. Z.; Cavalli, A.; Haverkort, J. E. M.; Bakkers, E. P. A. M.; Garnett, E. C. Quantifying Losses and Thermodynamic Limits in Nanophotonic Solar Cells. *Nat. Nanotechnol.* **2016**, *11*, 1071−1075.

(8) Cui, Y.; Van Dam, D.; Mann, S. A.; Van Hoof, N. J. J.; Van Veldhoven, P. J.; Garnett, E. C.; Bakkers, E. P. A. M.; Haverkort, J. E. M. Boosting Solar Cell Photovoltage *via* Nanophotonic Engineering. *Nano Lett.* **2016**, *16*, 6467−6471.

(9) Huang, Y.-F.; Chattopadhyay, S.; Jen, Y.-J.; Peng, C.-Y.; Liu, T.-A.; Hsu, Y.-K.; Pan, C.-L.; Lo, H.-C.; Hsu, C.-H.; Chang, Y.-H.; Lee, C.-S.; Chen, K.-H.; Chen, L.-H. Improved Broadband and Quasi-Omnidirectional Anti-Reflection Properties with Biomimetic Silicon Nanostructures. *Nat. Nanotechnol.* **2007**, *2*, 770−774.

(10) Poitras, D.; Dobrowolski, J. A. Toward Perfect Antireflection Coatings. 2. Theory. *Appl. Opt.* **2004**, *43*, 1286−1295.

(11) Peng, K.-Q.; Lee, S.-T. Silicon Nanowires for Photovoltaic Solar Energy Conversion. *Adv. Mater.* **2011**, *23*, 198−215.

(12) Tian, B. Z.; Kempa, T. J.; Lieber, C. M. Single Nanowire Photovoltaics. *Chem. Soc. Rev.* **2009**, *38*, 165−184.

(13) Garnett, E. C.; Brongersma, M. L.; Cui, Y.; McGehee, M. D. Nanowire Solar Cells. *Annu. Rev. Mater. Res.* **2011**, *41*, 269−295.

(14) Krogstrup, P.; Jørgensen, H. I.; Heiss, M.; Demichel, O.; Holm, J. V.; Aagesen, M.; Nygard, J.; Fontcuberta i Morral, A. Single-Nanowire Solar Cells Beyond the Shockley-Queisser Limit. *Nat. Photonics* **2013**, *7*, 306−310.

(15) Misra, S.; Yu, L. W.; Foldyna, M.; Roca i Cabarrocas, P. High Efficiency and Stable Hydrogenated Amorphous Silicon Radial Junction Solar Cells Built on VLS-Grown Silicon Nanowires. *Sol. Energy Mater. Sol. Cells* **2013**, *118*, 90−95.

(16) Sun, X. L.; Zhang, T.; Wang, J. Z.; Yang, F.; Xu, L.; Shi, Y.; Chen, K. J.; Roca i Cabarrocas, P.; Yu, L. W. Firmly Standing Three-Dimensional Radial Junctions on Soft Aluminum Foils Enable Extremely Low Cost Flexible Thin Film Solar Cells with Very High Power-to-Weight Performance. *Nano Energy* **2018**, *53*, 83−90.

(17) Wagner, R. S.; Ellis, W. C. Vapor-Liquid-Solid Mechanism of Single Crystal Growth. *Appl. Phys. Lett.* **1964**, *4*, 89.

(18) Tsakalakos, L.; Balch, J.; Fronheiser, J.; Korevaar, B. A.; Sulima, O.; Rand, J. Silicon Nanowire Solar Cells. *Appl. Phys. Lett.* **2007**, *91*, 233117.

(19) Martin, A. G. Third Generation Photovoltaics: Ultra-High Conversion Efficiency at Low Cost. *Prog. Photovoltaics* **2001**, *9*, 123−135.

(20) Yu, L. W.; Fortuna, F.; O'Donnell, B.; Patriache, G.; Roca i Cabarrocas, P. Stability and Evolution of Low-Surface-Tension Metal Catalyzed Growth of Silicon Nanowires. *Appl. Phys. Lett.* **2011**, *98*, 123113.

(21) Yu, L. W.; O'Donnell, B.; Maurice, J. L.; Roca i Cabarrocas, P. Core-Shell Structure and Unique Faceting of Sn-Catalyzed Siliconnanowires. *Appl. Phys. Lett.* **2010**, *97*, 23107.

(22) Yu, L. W.; O'Donnell, B.; Alet, P.-J.; Conesa-Boj, S.; Peiró, J.; Arbiol, F.; Roca i Cabarrocas, P. Plasma-Enhanced Low Temperature Growth of Silicon Nanowires and Hierarchical Structures by Using Tin and Indium Catalysts. *Nanotechnology* **2009**, *20*, 225604.

(23) Yu, L. W.; Alet, P.-J.; Picardi, G.; Maurin, I.; Roca i Cabarrocas, P. Synthesis, Morphology and Compositional Evolution of Silicon Nanowires Directly Grown on SnO2 Substrate. *Nanotechnology* **2008**, *19*, 485605.

(24) Yu, L. W.; Rigutti, L.; Tchernycheva, M.; Misra, S.; Foldyna, M.; Picardi, G.; Roca i Cabarrocas, P. Assessing Individual Radial Junction Solar Cells over Millions on VLS-Grown Silicon Nanowires. *Nanotechnology* **2013**, *24*, 275401.

(25) Alet, P.-J.; Yu, L. W.; Patriarche, G.; Palacin, S.; Roca i Cabarrocas, P. *In situ* Generation of Indium Catalysts to Grow Crystalline Silicon Nanowires at Low Temperature on ITO. *J. Mater. Chem.* **2008**, *18*, 5187−5189.

(26) Zardo, I.; Conesa-Boj, S.; Estradé, S.; Yu, L. W.; Peiro, F.; Roca i Cabarrocas, P.; Morante, J. R.; Arbiol, J.; Fontcuberta i Morral, A. Growth Study of Indium-Catalyzed Silicon Nanowires by Plasma Enhanced Chemical Vapor Deposition. *Appl. Phys. A: Mater. Sci. Process.* **2010**, *100*, 287−296.

(27) Yu, L. W.; Fortuna, F.; O'Donnell, B.; Jeon, T.; Foldyna, M.; Picardi, G.; Roca i Cabarrocas, P. Bismuth-Catalyzed and Doped Silicon Nanowires for One-Pump-Down Fabrication of Radial Junction Solar Cells. *Nano Lett.* **2012**, *12*, 4153−4158.

(28) Spadafora, E. J.; Demadrille, R.; Ratier, B.; Grévin, B. Imaging the Carrier Photogeneration in Nanoscale Phase Segregated Organic Heterojunctions by Kelvin Probe Force Microscopy. *Nano Lett.* **2010**, *10*, 3337−3342.

(29) Hoppe, H.; Glatzel, T.; Niggemann, M.; Hinsch, A.; Lux-Steiner, M. Ch.; Sariciftci, N. S. Kelvin Probe Force Microscopy Study on Conjugated Polymer/Fullerene Bulk Heterojunction Organic Solar Cells. *Nano Lett.* **2005**, *5*, 269−274.

(30) Glatzel, T.; Hoppe, H.; Sariciftci, N. S.; Lux-Steiner, M. Ch.; Komiyama, M. Kelvin Probe Force Microscopy Study of Conjugated Polymer/Fullerene Organic Solar Cells. *Jpn. J. Appl. Phys.* **2005**, *44*, 5370−5373.

(31) Giridharagopal, R.; Rayermann, G. E.; Shao, G.; Moore, D. T.; Reid, O. G.; Tillack, A. F.; Masiello, D. J.; Ginger, D. S. Submicrosecond Time Resolution Atomic Force Microscopy for Probing Nanoscale Dynamics. *Nano Lett.* **2012**, *12*, 893−898.

(32) Mikulik, D.; Ricci, M.; Tutuncuoglu, G.; Matteini, F.; Vukajlovic, J.; Vulic, N.; Alarcon-Llado, E.; Fontcuberta i Morra, A. Conductive-Probe Atomic Force Microscopy as a Characterization Tool for Nanowire-Based Solar Cells. *Nano Energy* **2017**, *41*, 566−572.

(33) Müller, M.; Hývl, M.; Kratzer, M.; Teichert, C.; Misra, S.; Foldyna, M.; Yu, L. W.; Roca i Cabarrocas, P.; Itoh, T.; Hájková, Z.; Vetushka, A.; Ledinský, M.; Kočka, J.; Fejfar, A. Investigating Inhomogeneous Electronic Properties of Radial Junction Solar Cells Using Correlative Microscopy. *Jpn. J. Appl. Phys.* **2015**, *54*, 08KA08.

(34) Yu, L. W.; Misra, S.; Wang, J. Z.; Qian, S. Y.; Foldyna, M.; Xu, J.; Shi, Y.; Johnson, E.; Roca i Cabarrocas, P. Understanding Light Harvesting in Radial Junction Amorphous Silicon Thin Film Solar Cells. *Sci. Rep.* **2015**, *4*, 4357.

(35) Lange, M.; Guénon, S.; Lever, F.; Kleiner, R.; Koelle, D. A High-Resolution Combined Scanning Laser and Widefield Polarizing Microscope for Imaging at Temperatures from 4 to 300 K. *Rev. Sci. Instrum.* **2017**, *88*, 123705.

(36) Shah, A. V.; Schade, H.; Vanecek, M.; Meier, J.; Vallat-Sauvain, E.; Wyrsch, N.; Kroll, U.; Droz, C.; Bailat, J. Thin-Film Silicon Solar Cell Technology. *Prog. Photovoltaics* **2004**, *12*, 113−142.

(37) Green, M. A. Thin-Film Solar Cells: Review of Materials, Technologies and Commercial Status. *J. Mater. Sci.: Mater. Electron.* **2007**, *18*, 15−19.

(38) Lu, J. W.; Qian, S. Y.; Yu, Z. W.; Misra, S.; Yu, L. W.; Xu, J.; Shi, Y.; Roca i Cabarrocas, P.; Chen, K. J. How Tilting and Cavity-Mode-Resonant Absorption Contribute to Light Harvesting in 3D Radial Junction Solar Cells. *Opt. Express* **2015**, *23*, A1288−A1296.